THE JOURNAL OF PHYSICAL CHEMISTRY LETTERS
A JOURNAL OF THE AMERICAN CHEMICAL SOCIETY

pubs.acs.org/JPCL Letter

Structural Reorganization of a Synthetic Mimic of the Oxygen-Evolving Center in Multiple Redox Transitions Revealed by Electrochemical FTIR Spectra

Mohan Wang, Ying Zhang, Changhui Chen, Chunxi Zhang, Junguang Jiang, and Yuxiang Weng*

Cite This: *J. Phys. Chem. Lett.* 2021, 12, 9830−9839 Read Online

ABSTRACT: In photosynthesis, the protein-bound natural oxygen-evolving center (OEC) undergoes multiple oxidation-state transitions in the light-driven water splitting reactions with a stepwise change in the oxidation potential. Because the protein is vulnerable to electrochemical oxidation, the multiple oxidation/reduction-state transitions can hardly be achieved by electrochemical oxidation with a continuous change in the oxidation potential. An OEC mimic that can undergo four redox transitions has been synthesized (Zhang, C., et al. *Science*, **2015**, *348*, 690−693). Here we report an electrochemical FTIR spectroscopic study of this synthetic complex at its multiple oxidation states in the low-frequency region for Mn−O bonds. Compared with those of the native OEC induced by pulsed laser flashes, our results also show the existence of two structural isomers in the S_2 state, with the closed cubane conformer being more stable than the open cubane conformer, in contrast to that of the native OEC in which the open form is more stable.

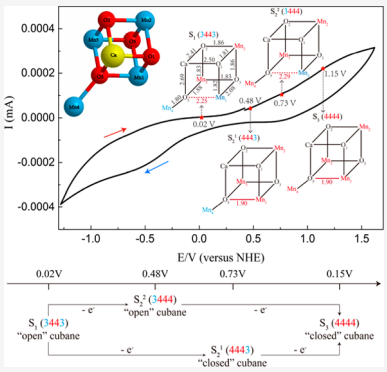

Light-driven water oxidation in nature is accomplished by photosystem II, where it is catalyzed by the oxygen-evolving complex (OEC), an oxo-bridged Mn_4CaO_5 cluster that accumulates four oxidizing equivalents and catalyzes the formation of dioxygen.[1−7] A photon-induced abstraction of an electron from the OEC occurs during each of the four state transitions of the catalytic cycle through five metastable storage states S_i (i = 0−4). Molecular O_2 is produced during the S_3−(S_4)−S_0 transition.[8−14]

Huge research efforts have been devoted to unveil these intermediates states in an effort to elucidate the detailed mechanism for the formation and release of the O_2 molecule, using spectroscopic techniques like extended X-ray absorption fine structure (EXAFS),[15] electron nuclear double resonance (ENDOR),[16] electron paramagnetic resonance (EPR),[17] FTIR,[18−20] X-ray crystallography,[21,22] and theoretical model studies.[23−27] It has been proposed that in the OEC, a μ-oxo O_5 is unusually far from the nearby Mn ions, suggesting weak binding and higher reactivity. Therefore, O_5 was proposed as a candidate for dioxygen formation.[5,21,28−34] Today, much information related to the mechanism of biological water oxidation is available; however, the information available at present is still insufficient to construct a full picture of the process of water oxidation with all of the mechanistic details, and the recent evidence points to the activated catalyst state requiring inherent structural flexibility.[35,36]

Among the various spectroscopic methods, vibrational spectroscopy has been used as an investigative tool to study the structure and mechanism of the OEC,[37] providing information about various aspects during the photocatalytic cycles. For example, absorbance changes in the vibrations of a water molecule in the OEC have been detected in the range of 2500−3700 cm^{-1} using H/D exchange studies.[38,39] Those in the range of 1200−1800 cm^{-1} are attributed to the vibrations of the protein residues ligated to the OEC,[18,38,40] and the low-frequency region in the range of 200−1000 cm^{-1} has been attributed to those of the Mn−ligand and Mn−O vibrations. The low-frequency spectra are very informative in revealing the structural changes of the OEC during the state transitions. Chu et al. were able to obtain IR difference spectra of the S_1−S_2 transition of the OEC in the range of 350−1000 cm^{-1}. They identified a Mn−O−Mn vibration at 625 cm^{-1} in the S_1 state, which shifts to 606 cm^{-1} after the transition to the S_2 state.[19,41,42]

Because of the lability of the protein-bound OEC that prevents electrochemical characterization and controlled modification of its structure and constituents for spectral assignments, vibrational spectra of synthetic model complexes are imperative to interpreting the IR and Raman spectra of the OEC. Several multinuclear Mn complexes have been synthesized to understand the spectral properties of the OEC. A summary of the low-frequency vibrational modes

Received: August 16, 2021
Accepted: September 30, 2021

https://doi.org/10.1021/acs.jpclett.1c02689
J. Phys. Chem. Lett. 2021, 12, 9830−9839

observed in these compounds is presented in a review by Babcock et al.[42] Along these lines,[43−45] in 2015 Zhang et al.[46] synthesized an artificial Mn_4CaO_4 cluster with a dangling Mn_4 atom, which was quite structurally similar with the natural OEC. Despite the absence of the second μ-oxo bridge between Mn_3 and Mn_4 in the structure, the artificial cluster can undergo four redox transitions and displays low-spin and high-spin EPR signals at low temperatures in the S_2 state prepared by chemical oxidation, similar as those in the natural OEC in which the two EPR signals and their respective spin states (g = 2 signal, $S = {}^1/_2$; g = 4.1−4.9 signals, $S \geq {}^3/_2$) have been proposed to arise from two OEC conformers differing in the localization of the Mn^{3+} ion in the S_2 state ($Mn_1^{3+}Mn_4^{4+}$ vs $Mn_1^{4+}Mn_4^{3+}$).[47] Therefore, the crystal structure of this artificial Mn_4CaO_4 cluster provides an excellent model for interpreting the spectroscopic signatures of the native OEC and a "calibration" for the computational approaches in the spectral analysis. To compare the IR spectra of the synthetic mimics with those of the OEC in the S_1 state, recently Tychengulova et al. performed normal-mode analysis (NMA) and effective normal-mode analysis (ENMA) calculations of this synthetic mimic, providing detailed assignments of the vibrational modes for the low vibrational frequencies from the MnO cluster and the higher frequencies from the ligand carboxylates.[27] Raucci et al. simulated oxygen−oxygen bond formation in this synthetic structure with a modification of some binding ligands substituted with water molecules.[48] Their results suggest that the key electronic features of the natural OEC reactivity are well reproduced in the synthetic compound. On the contrary, in contrast to the lability of the protein-bound OEC subjected to elctrochemical characterization, this molecular mimic can facilitate electrochemical preparation of various intermediates by direct control of the applied redox potentials; thus, it can provide spectroscopic signatures for the native OEC as well as the reaction mechanism for O—O bond formation.

In this work, the structural changes in the synthetic Mn_4CaO_4 cluster are characterized with FTIR difference spectra with its electrochemically prepared multiple oxidation states in the low-IR frequency region. In parallel to those of the natural OEC, our results also suggest that there are two different conformers in the S_2 state, i.e., an open and a closed cubane conformer, with the latter being slightly more thermodynamically stable than the former, which is the reverse of that of the OEC.[36,48]

Among the five intermediate states of the so-called Kok cycle during oxygen evolution of the OEC,[1] the most studied intermediate state of OEC is the S_2 state. Two distinct signals characterizing the S_2 state have been detected by EPR spectroscopy and assigned to two interconvertible conformers by quantum chemistry calculations.[47,49] These two structures show a 1:1 correspondence with the two EPR signals for the S_2 state,[50] i.e., one for an open cubane structure with a low-spin ground state (namely the S_2^A state, associated with a multiline EPR signal at g = 2.0, $S = {}^1/_2$) and the other for a closed cubane structure with a high-spin ground state (namely the S_2^B state, associated with an EPR signal at g = 4.1, $S = {}^5/_2$).[36,47] The "open" or "closed" cubane structures are defined by the distance between Mn_1 and O_5. For example, if this distance is short enough to form a Mn−O bond, a closed Mn_3CaO_4 cubane would be formed; otherwise, it remains in an "open" state as in the S_1 state. Crystal structures for the intermediate states detected by an X-ray free electron laser reveal that the Mn_1-O_5 distance of the OEC is 2.70 Å for the S_1 state, 2.79 Å for the S_2 state in the open cubane state, and 3.04 Å for the S_3 state.[34] Although there are still no direct structural data for the Mn_1-O_5 distance in the closed cubane structure of the S_2 state, density functional theory (DFT) calculations show a Mn_1-O_5 distance of 1.87−1.89 Å for the closed cubane in the S_2 state in contrast to a value of 3.21 (or 3.07) Å for the open cubane.[47,49,51] The open cubane structure is more stable by ∼1 kcal/mol (∼0.04 eV).[36,48]

For the synthetic complex, the $S_1 \rightarrow S_2$ transition has also been detected by cyclic voltammetry at a redox potential of ∼0.8 V versus the normal hydrogen electrode (NHE), and the value is close to the estimated potential of the corresponding native OEC redox transition (≥0.9 V).[4,52] In addition, the S_2 state of the synthetic complex was further prepared by chemical oxidation using $[Fe(phen)_3](PF_6)_3$ (phen, 1,10-phenanthroline) at a redox potential of +1.1 V versus the NHE, and two (low and high) spin EPR signals have been observed at low temperatures, which are similar to the low-spin (g = 2.0) and high-spin ($g \geq 4.1$) EPR signals observed in the S_2 state of the native OEC.[47,53,54] Later computer simulation of the ligand-modified synthetic compound reveals that the $S_1 \rightarrow S_2$ transition leads to the preferential oxidation of the Mn_4 atom, which is favored by ∼3 kcal/mol (∼0.13 eV) compared to that of the Mn_1 atom. This work further reveals that the synthetic compound also exists in open and closed conformers corresponding to whether Mn_4(III) is oxidized (open, S_2^A) or Mn_1(III) is oxidized (closed, S_2^B). The calculated Mn_1-O_5 distances for these two structures are 2.29 and 1.90 Å, respectively. The calculation further reveals that the closed conformer formed during the $S_1 \rightarrow S_2$ step has a Mn_3CaO_4 core that is more compacted than that of the S_1 state and that of the open conformer in the S_2 state.[48]

In contrast to the calculated structural change during the various oxidative states,[48] the IR spectra have been calculated in the S_1 state for the synthetic complex. In the assignment of the calculated IR spectra in the low-frequency region arising from the Mn_4CaO_4 cluster in the S_1 state of the synthetic complex,[27] they clearly assign the bands to the vibrational modes of specific Mn−O bonds, for example, the Mn_1-O_1 stretching mode at ∼608 cm^{-1}, the Mn_2-O_1 stretching mode at ∼643 cm^{-1}, the Mn_3-O_5 moiety stretching at 669 cm^{-1}, the Mn_2-O_3 bond stretching at 560 cm^{-1}, and the Mn_2-O_2 bond stretching at 490 cm^{-1}. Apparently, these theoretical assignments provide guidance for our currently experimentally observed IR difference spectra during the S_i-S_{i+1} transition.

The redox potential of the Ag/Ag^+ reference electrode in acetonitrile in the microelectrochemical cell was calibrated using ferrocenium/ferrocene ($Fc^{+/0}$) as the standard (0.71 V in acetonitrile),[55] which leads to an evaluated redox potential of 0.52 V for the Ag/Ag^+ electrode versus the NHE (see Supporting Information 1). The cyclic voltammograms (CVs) of the synthetic complex in acetonitrile measured within both the normal cells[46] and the microelectrochemistry cells both against the NHE are compared in Figure 1a. To avoid the interference from the electrolyte Bu_4NFP_6 in the low-frequency region, Bu_4NBF_4 was chosen to replace Bu_4NFP_6 (see Supporting Information 2). To better compare the fine structures for the redox potential peaks, secondary derivatives, which have an improved peak resolution generally used in the spectroscopic analysis,[56] are performed on these two CVs as shown in panels b and c of Figure 1. The redox peaks appear as negative peaks in the CV for the potential sweep from the negative to the positive (denoted in Figure 1b), while they

https://doi.org/10.1021/acs.jpclett.1c02689
J. Phys. Chem. Lett. 2021, 12, 9830−9839

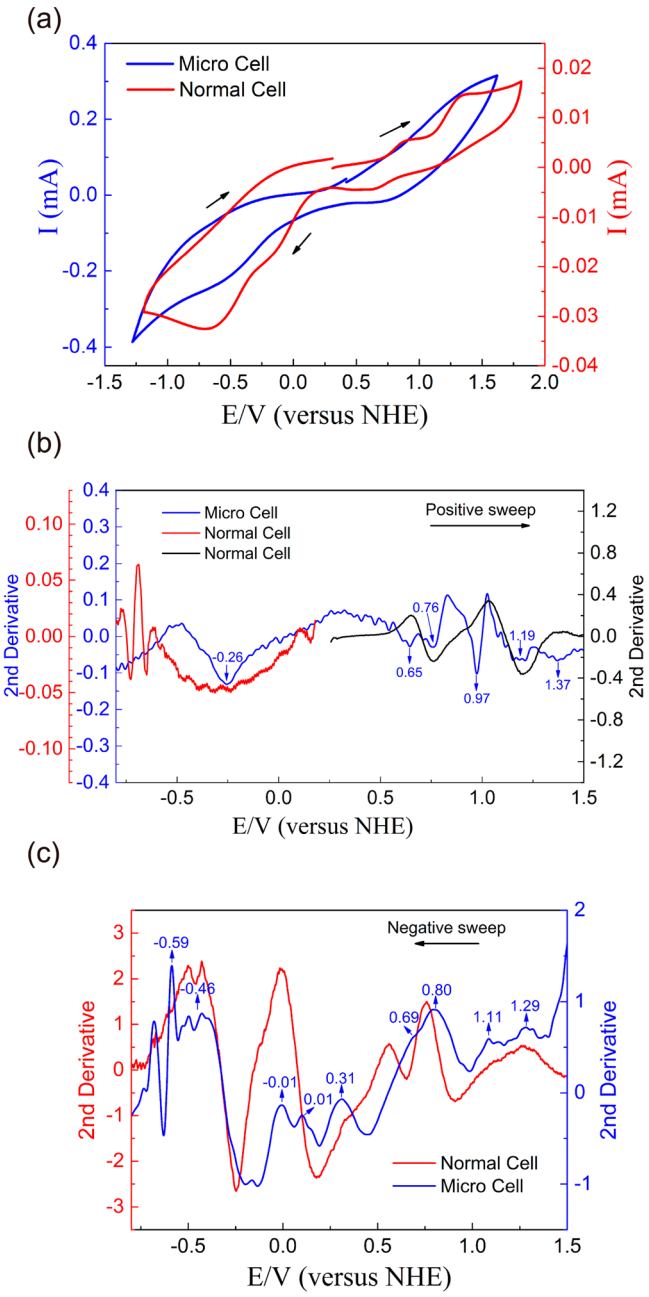

Figure 1. Comparisons of the cyclic voltammograms and their corresponding secondary derivatives for the synthetic complex in acetonitrile within normal (red or black line) and microelectrochemical (blue line) cells. (a) CV with potentials vs the NHE, at a scan rate of 100 mV/s. (b) Positive potential sweep. (c) Negative potential sweep. The secondary derivative CVs were obtained by performing the first-order derivative on the CV curves. After a proper data averaging to remove the high-frequency noise, the resulting data of the first derivative were used to perform the secondary derivative, while the high-frequency noises were also removed by data averaging.

appear as positive peaks for the potential sweep from the positive to the negative (denoted in Figure 1c). As shown in panels b and c of Figure 1, the secondary derivative peaks for CVs measured in both normal and microelectrochemical cells agree with each other in general. The peak values of the redox potential peaks appearing in different oxidation/reduction states during the potential sweep in both directions as well as the averaged midpoint potentials are summarized in Table 1.

Table 1. Summary of the Derived Redox Potentials in the Second Derivative and the Corresponding As-Acquired Cyclic Voltammograms

	redox potential (V) from the second derivative of the CV				
sweep direction	$S_{-1} \leftrightarrow S_0$	$S_0 \leftrightarrow S_1$	$S_1 \leftrightarrow S_2$	$S_2 \leftrightarrow S_3$	$S_3 \leftrightarrow S_4$
− → +	−0.26	0.04	0.65	0.97	1.37
			0.76	1.19	
+ → −	−0.46	−0.01	0.31	0.80	1.29
			0.69	1.11	
$E_{1/2\ \text{microcell}}$	−0.36	0.02	0.48	0.89	1.33
			0.73	1.15	
$E_{1/2\ \text{normal-cell}}$	−0.5	−0.1	0.80	1.25	NA

As reported previously, the cyclic voltammogram of the synthetic complex shows averaged redox potentials in acetonitrile for $S_{-1} \rightarrow S_0$ at −0.5 V, $S_0 \rightarrow S_1$ at −0.1 V, $S_1 \rightarrow S_2$ at 0.8 V, and $S_2 \rightarrow S_3$ at 1.25 V.[46] As shown in Table 1, the midpoint redox potentials derived by the secondary derivative on CV exhibit striking fine features for the $S_1 \leftrightarrow S_2$ and $S_2 \leftrightarrow S_3$ transitions, for they consist of a doublet peak with a splitting width of approximately 0.2−0.3 V. We have shown that these splitting peaks are not arising from either the solvent or the added electrolytes (Figure S2). Therefore, we denote these two subtransitions in $S_1 \rightarrow S_2$ as $S_1 \rightarrow S_2^1$ for the lower oxidation peak with an $E_{1/2}$ of 0.48 V and $S_1 \rightarrow S_2^2$ for a higher oxidation peak with an $E_{1/2}$ of 0.73 V. Accordingly, with respect to $S_2 \rightarrow S_3$, we denote $S_2^1 \rightarrow S_3$ with an $E_{1/2}$ of 0.89 V and $S_2^2 \rightarrow S_3$ with an $E_{1/2}$ of 1.15 V. We use superscript numerals 1 and 2 to denote these two conformers in contrast to S_2^A and S_2^B for the native OEC.

Figure 2 shows electro-oxidation-induced difference spectra of various S-state transitions in the low-frequency Mn−O vibrational region of the synthetic Mn cluster, including $S_0 \rightarrow S_1$ (S_1/S_0), $S_1 \rightarrow S_2^1$ (S_2^1/S_1), $S_1 \rightarrow S_2$ (S_2/S_1), and $S_2^2 \rightarrow S_3$ (S_3/S_2^2). Figure 2a reveals that there is almost no obvious spectral change during the $S_0 \rightarrow S_1$ and $S_1 \rightarrow S_2^1$ transitions during the oxidation sweep, while significant spectral changes occur during the $S_1 \rightarrow S_2$ and $S_2^2 \rightarrow S_3$ transitions characterized by a bleaching peak around 604 cm^{-1} and an absorption peak around 622 cm^{-1}. The corresponding difference spectra of the reversed processes, i.e., reduction sweep, are shown in Figure 2b. Because of the overpotential at the electrodes, the difference IR spectra of the various S-state transitions are not reversed at a given applied potential.

As shown in Figure 2a, the IR absorbance difference spectra for $S_1 \rightarrow S_2^1$ are almost like a baseline during the potential sweep. To obtain a better IR absorbance difference spectra for $S_1 \rightarrow S_2^1$, we fixed the oxidation electrode potential at 0.62 V close to that of $S_1 \rightarrow S_2^1$ (0.65 V) to initiate a slow oxidation of $S_1 \rightarrow S_2^1$, and the IR difference spectra are taken as those between the end and start of the oxidation process with a quite long reaction time. The IR difference spectra for the reversed process are obtained by setting the electrode potential at 0.42 V ($S_1 \leftarrow S_2^1$, 0.31 V).

The corresponding IR absorbance difference spectra acquired at the fixed potential for the forward and backward reaction processes in the low- and high-frequency regions are shown in Figure 3, while those for the middle-frequency regions are shown in Figure S3.

As revealed obviously in these figures, all of the difference absorbance peaks within the spectral region from 440 to 1800 cm^{-1} are almost reversible when the electrode reaction is

https://doi.org/10.1021/acs.jpclett.1c02689
J. Phys. Chem. Lett. 2021, 12, 9830−9839

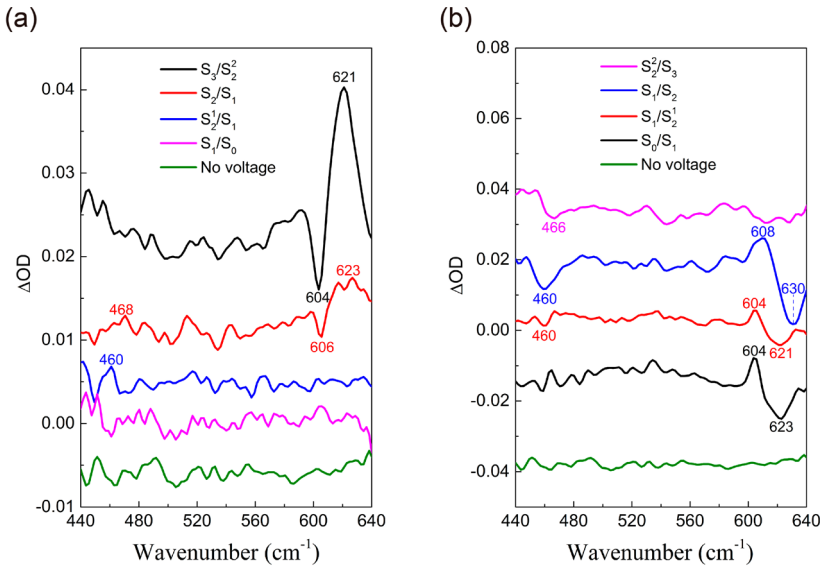

Figure 2. IR difference spectra at a fixed electrode potential in the low-frequency region at different oxidation and reduction multistates. (a) During the oxidation sweep, where the fixed electrode potentials are indicated in parentheses: S_3/S_2^2 (1.23 V/1.02 V), S_2/S_1 (0.82 V/0.62 V), S_2^1/S_1 (0.72 V/0.12 V), and S_1/S_0 (0.12 V/−0.28 V). (b) During the reduction sweep, where the fixed electrode potentials are indicated in parentheses: S_2^2/S_3 (0.82 V/1.25 V), S_1/S_2 (0.62 V/0.82 V), S_1/S_2^1 (0.02 V/0.42 V), and S_0/S_1 (−0.28 V/0.12 V).

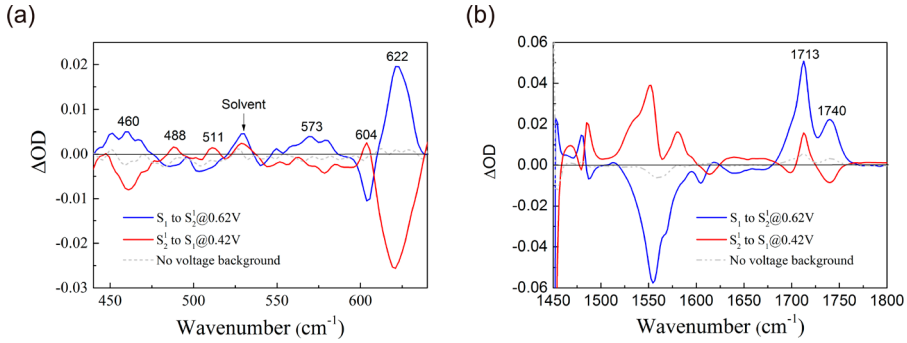

Figure 3. IR difference spectra in the low-frequency region for $S_1 \rightarrow S_2^1$ (blue) and $S_2^1 \rightarrow S_1$ (red) at fixed applied potentials of 0.62 and 0.42 V, respectively, in the (a) low-frequency and (b) high-frequency regions. The difference spectrum of $S_1 \rightarrow S_2^1$ was obtained by subtracting the IR spectrum collected at the 60th second from the IR spectrum collected at the 2500th second. The difference spectrum of $S_2^1 \rightarrow S_1$ was obtained by subtracting the IR spectrum collected at the 60th second from the IR spectrum collected at the 2900th second.

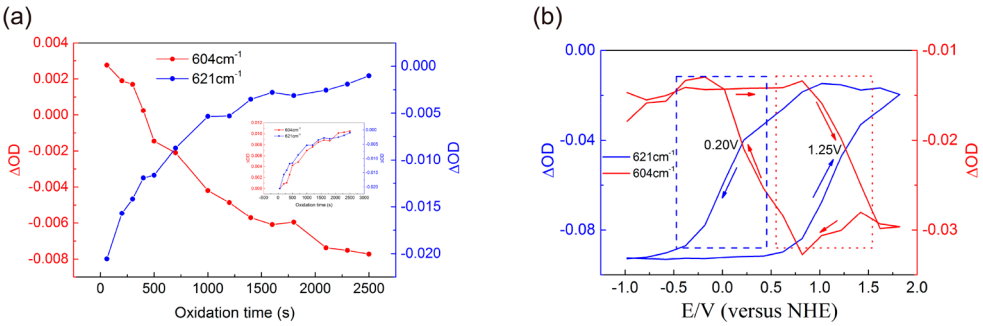

Figure 4. IR intensity change kinetics and IR intensity-detected cyclic voltammograms for 604 and 621 cm^{-1} during the $S_1 \rightarrow S_2^1$ transition. (a) IR intensity kinetics and comparison of inverted kinetics at 604 cm^{-1} with as-acquired kinetics at 621 cm^{-1}. (b) IR intensity-detected cyclic voltammograms acquired at 604 and 621 cm^{-1}.

reversed from the oxidation to the reduction process, except for those around 530 and 1713 cm^{-1}, where the former is tentatively assigned to the one that arises from the solvent or electrolyte, with the latter arising from the carbonyl group in the pivalic acid[57,58] (1713 and 1740 cm^{-1} can be from a pair of pivalic acids). A prominent feature in the low-frequency region during the $S_1 \rightarrow S_2^1$ transition is the emergence of the absorption bands at around 460 and 622 cm^{-1} accompanied by a bleaching peak at 604 cm^{-1}.

According to the IR spectral calculation, the $Mn_1(III)-O_1$ bond (1.84 Å) has an absorption at 608 cm^{-1},[27] and when $Mn_1(III)$ is oxidized to $Mn_1(IV)$, the corresponding

https://doi.org/10.1021/acs.jpclett.1c02689
J. Phys. Chem. Lett. 2021, 12, 9830−9839

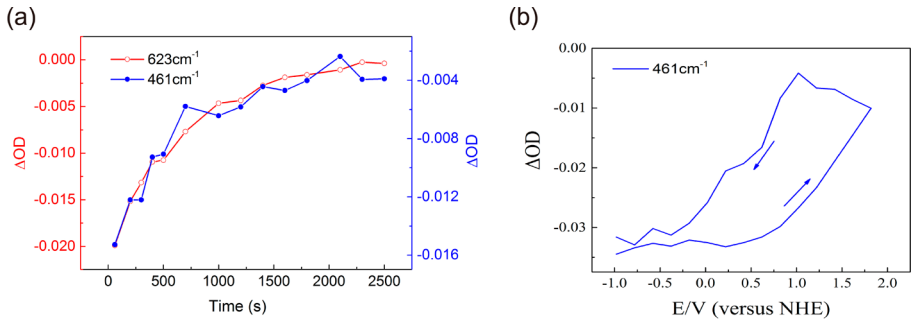

Figure 5. IR intensity kinetics and IR intensity-detected cyclic voltammograms for 461 cm^{-1}. (a) Comparison of the IR intensity kinetics at 461 cm^{-1} with that at 623 cm^{-1}. (b) IR intensity-detected cyclic voltammogram acquired at 461 cm^{-1}.

$Mn_1(IV)-O_1$ bond length is decreased to 1.81 Å in a calculated S_2 state,[48] leading to a tighter Mn−O bond. Therefore, it is expected that the IR absorption peak would have a certain amount of blue shift when $Mn_1(III)-O_1$ is oxidized to $Mn_1(IV)-O_1$ during the $S_1 \rightarrow S_2^1$ transition. Thus, we assign the 604 cm^{-1} bleaching band to the $Mn_1(III)-O_1$ stretching in the S_1 state and 622 cm^{-1} to the $Mn_1(IV)-O_1$ in the S_2^1 state of the synthetic complex. To further reveal the structural correlation between the 604 and 622 cm^{-1} bands, we inspected the corresponding IR absorption intensity change kinetics during the $S_1 \rightarrow S_2^1$ transition as well as the IR intensity-detected cyclic voltammograms at 604 and ∼622 cm^{-1}, respectively, as shown in Figure 4.

During the $S_1 \rightarrow S_2^1$ transition, if $Mn_1(III)-O_1$ is converted to $Mn_1(IV)-O_1$, it is expected that the intensity change of the 604 cm^{-1} peak would be inversely correlated to that of 622 cm^{-1} accordingly. As shown in Figure 4a, the kinetics at 604 and 622 cm^{-1} are indeed inversely correlated, and they are almost superimposed if one of the kinetics is reversed (see the inset of Figure 4a). This inverse correlation also appears in their IR intensity-detected cyclic voltammograms marked by two rectangle boxes in blue and red within the different applied potential regions as shown in Figure 4b. Within each box, there is a curve crossing point located at 0.20 and 1.25 V, respectively. The patterns of the IR intensity-detected cyclic voltammograms clearly indicate that the electrode potential-induced intensity changes for 622 and 604 cm^{-1} bands are inversely correlated in both the oxidation and reduction processes. The facts strongly support the assignment of 604 and 622 cm^{-1} to the $Mn_1(III)-O_1$ and $Mn_1(IV)-O_1$ bonds, respectively.

Then we inspected another emerging band at ∼460 cm^{-1} during the $S_1 \rightarrow S_2^1$ transition. We found that its kinetics almost follows that of 622 cm^{-1} in Figure 5a, and its cyclic voltammogram in Figure 5b shares a similar feature at 622 cm^{-1} (Figure 4b, i.e., a typical oxidation-induced band formation). Visser et al. have shown that Mn−O vibrational modes can also be found in the low-frequency region as in the range of 520−425 cm^{-1}.[9] Considering this low spectral region for the Mn−O bond together with its association with $Mn_1(III)$ oxidation, this fact suggests the formation of a new $Mn_1(IV)-O$ bond. It has been shown that the metal−oxo bond length affects the cluster frequencies with a general trend that a decreasing Mn−O stretching frequency is correlated to an increasing bond length.[27] With reference to the correlation between the known Mn−O bond length and the calculated IR absorption peak, e.g., $Mn_1(III)-O_3$ with a bond length of 2.014 Å correlated with an absorption at 450 cm^{-1}, $Mn_2(IV)-O_2$ with a bond length of 1.876 Å correlated with an IR absorption at ∼490 cm^{-1}, and $Mn_3(IV)-O_3$ with a bond length of 1.862 Å in S_1 correlated with an absorption at ∼525 cm^{-1},[27] this newly formed $Mn_1(IV)-O$ with an absorption band at 460 cm^{-1} would have a bond length close to 1.88 Å. With respect to the proposed model of the S_2 state for the natural or synthetic complex,[48] the newly formed $Mn_1(IV)-O$ bond would correspond to $Mn_1(IV)-O_5$ bond formation in the closed conformers, where the calculated $Mn_1(IV)-O_5$ bond length for the closed cubane conformer in S_2^B of the OEC is ∼1.89 Å[51] and that of the artificial synthetic compound is 1.90 Å.[47,48] Interestingly, the calculated vibrational frequency for this $Mn_1(IV)-O_5$ bond in the OEC is 461 cm^{-1},[59] coinciding well with the observed value in the synthetic complex. Furthermore, Chu et al. have observed an absorption peak around 468 cm^{-1} when the S_1 state is oxidized to the S_2 state for the OEC.[41] These facts give further support to our assignment.

We further inspected the IR difference absorption spectra for the $S_2^1 \rightarrow S_2^2$ and $S_2^2 \rightarrow S_3$ transitions in Figure 2a and found that the spectral features are almost similar to those for the $S_1 \rightarrow S_2^1$ transition (Figure 3a) except for the absorption peak at 622 cm^{-1} in the $S_2^1 \rightarrow S_2^2$ transition is blue-shifted to 630 cm^{-1} in the reversed process as shown in Figure 2b. The oxidation-induced formation of the 460 and 622 cm^{-1} bands is further confirmed by the chemical oxidation of the synthetic complex by $[Fe(phen)_3](PF_6)_3$[46] (Figure S4).

For the native OEC, the S_2 state has been proposed to have two different interconvertible structures, i.e., an open cubane structure denoted as S_2^A $[Mn_4(IV)]$ and a closed cubane structure denoted as S_2^B $[Mn_1(IV)]$. The two structures have similar energies, with the open cubane structure being more stable by ∼1 kcal/mol.[36,47−49] A very similar result has been obtained via the DFT calculation of the ligand-modified synthetic complex by Raucci et al.;[48] their results reveal that the $S_1 \rightarrow S_2$ transition leads to the preferential oxidation of the $Mn_4(III)$ atom favored by ∼3 kcal/mol in terms of free energy. Furthermore, the Mn_1 oxidation leads to a cubane structure that is more compact than that obtained when Mn_4 is oxidized.[48]

Obviously, our observed facts at an electrode potential of 0.62 eV, a value slightly below the averaged peak potential for $S_1 \rightarrow S_2^1$, are consistent with the theoretical study in the following respects. (1) An IR absorbance decrease at the peak of 604 cm^{-1} induced by the slow oxidation suggests the oxidation of $Mn_1(III)-O_1$ to $Mn_1(IV)-O_1$. (2) The accompanying appearance of the 622 cm^{-1} band is attributed to the formation of $Mn_1(IV)-O_1$ from $Mn_1(III)-O_1$, where

https://doi.org/10.1021/acs.jpclett.1c02689
J. Phys. Chem. Lett. 2021, 12, 9830−9839

Table 2. Typical Low-Frequency Vibrational Modes and Their Possible Assignments of the Synthetic Complex and OEC

Synthetic Mn_4CaO_4 Cluster		OEC	
IR absorption peak (S_2/S_1)	Assignment	IR absorption peak (S_2/S_1)	Assignment
460 cm^{-1} (+)	Mn_1(IV)-O_5	468 cm^{-1} (+)[41]	Mn_1(IV)-O_5-Mn_3(IV) in S_2^B for 461 cm^{-1}[59] Mn_2(IV)-O_3-Mn_3(IV) in S_2^B for 466 cm^{-1}[59]
604 cm^{-1} (-)	Mn_1(III)-O_1	606 cm^{-1} (+)[68]	Mn(IV)-O-Mn(IV)[68] or 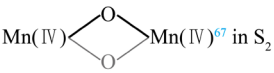 Mn(IV)[67] in S_2
622 cm^{-1} (+)	Mn_1(IV)-O_1	625 cm^{-1} (-)[68]	Mn(III)-O-Mn(IV)[68] or 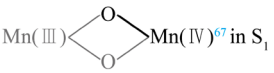 Mn(IV)[67] in S_1

the corresponding spectral blue shift in the absorption peak can be ascribed to a more compact arrangement of the Mn core leading to a decreased bond length. (3) Importantly, the simultaneous emergence of a new band at 460 cm^{-1} corresponds to the formation of the Mn_1(IV)−O_5 bond in a closed cubane configuration. The only discrepancy is that $S_1 \rightarrow S_2^1$ in our experiment corresponds to an oxidation-induced formation of a closed cubane conformer, which is equivalent to S_2^B in the native OEC. This indicates that the oxidation of Mn_1(III) is more preferable than that of Mn_4(III), which leads to the formation of a closed cubane in the synthetic complex. With reference to the DFT calculation and the counterpart in the native OEC, the S_2^2 conformer can be assigned as the open cubane conformer, and the S_2^1 state would be more favorable by an energy difference of ∼0.25 eV than S_2^2. This tendency is reversed in contrast to that of the theoretical study of the ligand-modified synthetic complex, as well as to S_2^A and S_2^B in the OEC. Such a discrepancy can be attributed to the structural difference in the model used in the DFT calculation. Comparison of the IR difference spectra of $S_2 \rightarrow S_3$ with those of $S_1 \rightarrow S_2$ in Figure 2 reveals that the features of the corresponding difference spectra for both transitions are quite similar, i.e., the bleaching at 604 cm^{-1} accompanied by an increased intensity at 460 and 622 cm^{-1}, respectively. In the laser flash-induced[60] and chemical oxidation-induced[41] S_2-minus-S_1 spectrum (S_2/S_1), Chu et al. also found the intensity changes in the low-frequency IR modes, i.e., positive bands at 631 and 468 cm^{-1}, respectively. They observed positive bands at 621 and 488 cm^{-1}, respectively, in the laser flash-induced S_3-minus-S_2 difference spectrum. These spectral features are in accordance with what we have observed for the synthetic complex,[60] which may suggest that even for the OEC, it is possible that a closed cubane structure in the S_2 and S_3 states can be formed in the solution phase.

We also noted that in the $S_1 \rightarrow S_2^1$ oxidation kinetics, the broad absorption band for the carboxylate asymmetric vibrational mode around 1550 cm^{-1} follows that of 604 cm^{-1} as shown in Figure S5, suggesting the effect of the change in the valence state in Mn_1 on the carboxylate ligand. It has been reported that the asymmetric and symmetric vibrational frequencies of carboxylate and their difference are affected by the two coordinated cations and their respective valence states. Because of the spectral overlap of the different carboxylate ligands, their intensity changes in the synthetic complex during oxidation process can be very complicated (Figure S3b). With reference to the calculated frequencies, the 1550 cm^{-1} band can be tentatively assigned to that of Z2,[27] which bridges Mn_4 and Mn_1. Although we did not intend to resolve either the frequency shifts or the respective intensity changes for various carboxylate ligands, we include the corresponding cyclic IR intensity change graphs and difference spectra during state transitions in Figures S3b and S5b.

For the OEC, earlier experimental data provide evidence that the closed cubane conformer should be an intermediate state toward the formation of the S_3 state,[49,61,62] though the structure of the S_3 state was finally found to be consistent with a Mn_4CaO_5 cluster arranged in an open cubane fashion.[17,26,31,63] Apparently, our results indicate a stable and closed cubane structure in the S_3 state for the synthetic complex, which is different from that in the OEC. We attribute such a difference to their structural difference, because there are no water molecules as the ligands in the synthetic complex, while the binding water molecules play an important role during the structural rearrangement for the OEC.[33−36]

We noted that our observed IR peak intensity changes for 622/604 cm^{-1} versus the redox potential during the S_1 to S_2 transition are just the opposite of those observed in the OEC. Chu et al. were able to obtain IR difference spectra of the S_1 to S_2 transition of the OEC in the range of 350−1000 cm^{-1}.[18,19,42] They identified a Mn−O−Mn vibration at 625 cm^{-1} in the S_1 state, which shifts to 606 cm^{-1} in the S_2 state.[68] A downward shift for a transition is supposed to correspond to a Mn(III) to Mn(IV) oxidation. Later upon ^{13}C isotope labeling, Kimura et al. found that the 616(−) and 605(+) cm^{-1} band peaks were downshifted by 2 cm^{-1}, indicating that these bands correspond to the vibrational modes of carbon-containing groups. Although these bands cannot be unequivocally assigned, they suggested that both modes derived from the carbon-containing groups [carboxylato(s) or atoms derived from an amino acid side chain] and the Mn−O−Mn modes are cumulatively induced in this region.[64] It has also been suggested that the μ-oxo atom in the Mn−O−Mn moiety responsible for the vibrational mode at 604/606 cm^{-1} is a substrate oxygen, tentatively assigned to the O_5 μ-oxo.[65,66] Other causes can be the changes in the symmetry of the OEC structure upon oxidation, and it is possible that these two bands are not the same vibrational modes and are from entirely different symmetry representations. On the basis of normal-mode analysis of the synthetic dioxo-bridged manganese dimers with their configuration simplified as a Mn_2O_2 diamond, Hasegawa et al. further suggested that the S_1 band at 625 cm^{-1} and the S_2 band at 606 cm^{-1} are assigned to the Mn(IV)−O asymmetric stretch (B_2 symmetry) in the dioxo-bridged Mn(III)Mn(IV) dimer moiety in the S_1-state Mn

https://doi.org/10.1021/acs.jpclett.1c02689
J. Phys. Chem. Lett. 2021, 12, 9830−9839

cluster core and the Mn−O−Mn asymmetric stretch (B_{3u} symmetry) in the dioxo-bridged Mn(IV)Mn(IV) dimer moiety in the OEC, respectively.[67] Therefore, the suggestion that the band shifts from 625 to 606 cm^{-1} during the S_1 to S_2 transition may be an oversimplification.[9] A comparison of the typical low-frequency vibrational modes and their possible assignments between the synthetic complex and OEC are listed in Table 2.

The synthetic Mn_4CaO_4 cluster of Zhang et al. resembles the native OEC not only in the ground-state structure but also in the multiple intermediate states. Because of its chemical stability under electrochemical oxidation and free of spectral interference from the amino acid side chains in IR spectra in contrast to the natural OEC, it provides a model complex for tracing the structural flexibility and rearrangement during the various state transitions for an electrochemical FTIR spectroscopic study. In addition to the spectroscopic method, other experimental methods with more straightforward information regarding the structural change will be necessary in the future. Our current findings are summarized as follows.

(1) Two oxidation−reduction potential peaks have been observed during the S_1 to S_2 transitions, i.e., a midpoint reduction potential at 0.48 V in acetonitrile (NHE) for the $S_1 \rightarrow S_2^1$ transition, where S_2^1 is assigned as a closed cubane conformer, and at 0.73 V for the $S_1 \rightarrow S_2^2$ transition, where S_2^2 is assigned as an open cubane conformer. On the basis of the assignment of the IR difference spectra, these two conformers are structurally similar to those two different conformers in the S_2 state in the OEC; i.e., S_2^1 corresponds to S_2^B (high spin, closed cubane), and S_2^2 to S_2^A(low spin, open cubane). The schematic structural diagrams for two S_2 conformers for the synthetic complex and OEC are shown in Figure 6. However,

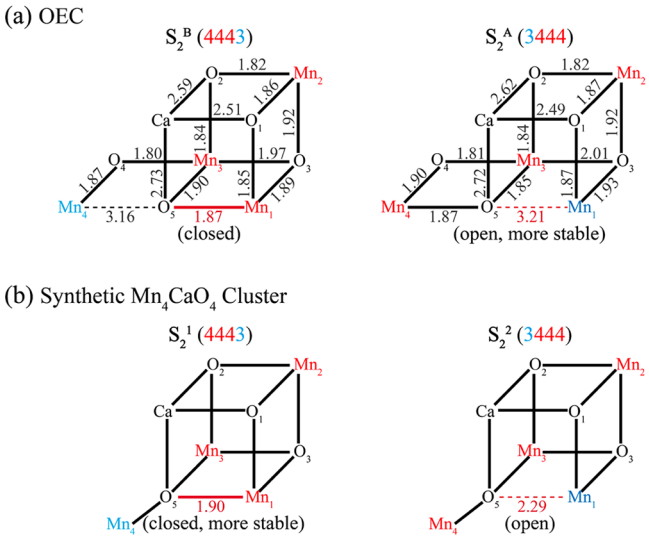

Figure 6. Structures for two S_2 conformers of both the OEC and the synthetic complex. (a) Closed cubane conformer (S_2^B) and open cubane conformer (S_2^A) of the OEC. (b) Closed cubane conformer (S_2^1) and open cubane conformer (S_2^2) of the synthetic complex.

for the synthetic complex, the closed cubane conformer is more stable than the open cubane conformer by ∼0.25 eV from our data; this is possibly because of their structural difference, because the synthetic complex does not contain any water molecules as the ligands.

(2) The respective oxidation−reduction potential for $S_2^1 \rightarrow S_3$ occurs at 0.89 V (NHE), and that for $S_2^2 \rightarrow S_3$ at 1.15 V (NHE).

(3) During the $S_1 \rightarrow S_2^1$ transition in the low-frequency region, we observed a decrease in intensity at 604 cm^{-1} that is correlated to the increase in intensity at 622 and 460 cm^{-1}, and such a tendency continues for the S_2 to S_3 transition. With respect to the DFT-calculated vibrational modes for the synthetic complex, the 604 cm^{-1} band is assigned to the $Mn_1(IV)-O_1$ bond in the S_1 state, the 622 cm^{-1} band to the $Mn_1(IV)-O_1$ bond in the S_2 state, and the 460 cm^{-1} band to a newly formed $Mn_1(IV)-O_5$ bond in the closed conformer of the S_2 state.

(4) In the S_3 state, the open and closed cubane conformers are converted to the closed cubane structure.

EXPERIMENTAL SECTION

The preparation of the synthetic complex $[Mn_4CaO_4(Bu^tCO_2)_8(Bu^tCO_2H)_2(C_5H_5N)]$ has been reported previously.[46] Electrochemical reactions were performed using an electrochemical workstation (CHI600E, from CH Instruments). The electrochemical cell is a homemade airtight three-electrode spectroelectrochemical cell. A Pt gauze (Pt wire, Φ 0.05 mm) was used as the working electrode. The counter electrode was a Pt wire (Φ 0.05 mm). A Ag wire (Φ 0.10 mm) was used as the quasi-reference electrode. The apparatus consists of a three-electrode spectroelectrochemical cell, IR transparent windows of the spectroelectrochemical cell were two commercial diamond plates (Φ 10 × 1 mm) produced by chemical vapor deposition (CVD). A perfluoroether O-ring (50 μm thick) was placed between the two diamond plates. Prior to each experiment, 2 mL of an electrolyte solution (0.1 M Bu_4NBF_4 in ultradry 1,2-dichloroethane) was purged with pure argon gas for 20 min. Before flowing into the electrolyte solution, argon gas first bubbled through ultradry 1,2-dichloroethane to minimize evaporation and small concentration changes in the electrolyte solution. In a glovebox under a constant purge of argon gas, the synthetic Mn_4CaO_4 complex was dissolved in a well-degassed electrolyte solution to a concentration of 5 mM and then sealed in the spectroelectrochemical cell. The FTIR spectrometer was a model VERTEX 80V instrument (Bruker) equipped with a DTGS detector working at room temperature. The compartment for spectral measurement was vacuumized. For each spectrum, a 128-scan interferogram was collected in a single-beam mode with a 4 cm^{-1} resolution.

ASSOCIATED CONTENT

Supporting Information

The Supporting Information is available free of charge at https://pubs.acs.org/doi/10.1021/acs.jpclett.1c02689.

Additional experimental details, data, and design for the microelectrochemical cell (PDF)

AUTHOR INFORMATION

Corresponding Author

Yuxiang Weng − *Laboratory of Soft Matter Physics, Institute of Physics, Chinese Academy of Sciences, Beijing 100190, China; University of Chinese Academy of Sciences, Beijing 100049, China; Songshan Lake Materials Laboratory, Dongguan, Guangdong 523000, China;* orcid.org/0000-0003-0423-2266; Email: yxweng@iphy.ac.cn

https://doi.org/10.1021/acs.jpclett.1c02689
J. Phys. Chem. Lett. 2021, 12, 9830−9839

Authors

Mohan Wang − *Laboratory of Soft Matter Physics, Institute of Physics, Chinese Academy of Sciences, Beijing 100190, China; University of Chinese Academy of Sciences, Beijing 100049, China*

Ying Zhang − *Laboratory of Soft Matter Physics, Institute of Physics, Chinese Academy of Sciences, Beijing 100190, China; University of Chinese Academy of Sciences, Beijing 100049, China;* orcid.org/0000-0003-2527-9397

Changhui Chen − *Laboratory of Photochemistry, Institute of Chemistry, Chinese Academy of Sciences, Beijing 100190, China*

Chunxi Zhang − *Laboratory of Photochemistry, Institute of Chemistry, Chinese Academy of Sciences, Beijing 100190, China;* orcid.org/0000-0002-8483-6897

Junguang Jiang − *State Key Laboratory of Electroanalytical Chemistry, Changchun Institute of Applied Chemistry, Chinese Academy of Sciences, Changchun, Jilin 130022, China*

Complete contact information is available at:
https://pubs.acs.org/10.1021/acs.jpclett.1c02689

Notes

The authors declare no competing financial interest.

■ ACKNOWLEDGMENTS

The authors thank the National Natural Science Foundation of China (21433014 and 91961203) and the Chinese Academy of Sciences Frontier Science Key Programs (QYZDJ-SSW-SYS017) for financial support.

■ REFERENCES

(1) Kok, B.; Forbush, B.; Mcgloin, M. Cooperation of Charges in Photosynthetic O_2 Evolution−I. A Linear Four Step Mechanism. *Photochem. Photobiol.* **1970**, *11*, 457−475.

(2) McEvoy, J. P.; Brudvig, G. W. Water-Splitting Chemistry of Photosystem II. *Chem. Rev.* **2006**, *106*, 4455−4483.

(3) Yano, J.; Yachandra, V. Mn_4Ca Cluster in Photosynthesis: Where and How Water is Oxidized to Dioxygen. *Chem. Rev.* **2014**, *114*, 4175−4205.

(4) Dau, H.; Zaharieva, I. Principles, Efficiency, and Blueprint Character of Solar-Energy Conversion in Photosynthetic Water Oxidation. *Acc. Chem. Res.* **2009**, *42*, 1861−1870.

(5) Cox, N.; Pantazis, D. A.; Neese, F.; Lubitz, W. Biological Water Oxidation. *Acc. Chem. Res.* **2013**, *46*, 1588−1596.

(6) Krewald, V.; Retegan, M.; Cox, N.; Messinger, J.; Lubitz, W.; Debeer, S.; Neese, F.; Pantazis, D. A. Metal Oxidation States in Biological Water Splitting. *Chem. Sci.* **2015**, *6*, 1676−1695.

(7) Retegan, M.; Krewald, V.; Mamedov, F.; Neese, F.; Lubitz, W.; Cox, N.; Pantazis, D. A. A Five-Coordinate Mn(IV) Intermediate in Biological Water Oxidation: Spectroscopic Signature and a Pivot Mechanism for Water Binding. *Chem. Sci.* **2016**, *7*, 72−84.

(8) Krewald, V.; Neese, F.; Pantazis, D. A. Implications of Structural Heterogeneity for the Electronic Structure of the Final Oxygen-Evolving Intermediate in Photosystem II. *J. Inorg. Biochem.* **2019**, *199*, 110797.

(9) Visser, H.; Dube, C. E.; Armstrong, W. H.; Sauer, K.; Yachandra, V. K. FTIR Spectra and Normal-Mode Analysis of a Tetranuclear Manganese Adamantane-Like Complex in Two Electrochemically Prepared Oxidation States: Relevance to the Oxygen-Evolving Complex of Photosystem II. *J. Am. Chem. Soc.* **2002**, *124*, 11008−11017.

(10) Debus, R. J. The Manganese and Calcium Ions of Photosynthetic Oxygen Evolution. *Biochim. Biophys. Acta, Bioenerg.* **1992**, *1102*, 269−352.

(11) Witt, H. T. Primary Reactions of Oxygenic Photosynthesis. *Ber. Bunsenges. Phys. Chem.* **1996**, *100*, 1923−1942.

(12) Hoganson, C. W.; Babcock, G. T. Mechanistic Aspects of the Tyrosyl Radical-Manganese Complex in Photosynthetic Water Oxidation. *Met. Ions Biol. Syst.* **2000**, *37*, 613−656.

(13) Renger, G. Photosynthetic Water Oxidation to Molecular Oxygen: Apparatus and Mechanism. *Biochim. Biophys. Acta, Bioenerg.* **2001**, *1503*, 210−228.

(14) Yamanari, T.; Kimura, Y.; Mizusawa, N.; Ishii, A.; Ono, T. A. Mid- to Low-frequency Fourier Transform Infrared Spectra of S-State Cycle for Photosynthetic Water Oxidation in Synechocystis sp. PCC 6803. *Biochemistry* **2004**, *43*, 7479−7490.

(15) Grundmeier, A.; Dau, H. Structural Models of the Manganese Complex of Photosystem II and Mechanistic Implications. *Biochim. Biophys. Acta, Bioenerg.* **2012**, *1817*, 88−105.

(16) Krewald, V.; Retegan, M.; Neese, F.; Lubitz, W.; Pantazis, D. A.; Cox, N. Spin State as a Marker for the Structural Evolution of Nature's Water-Splitting Catalyst. *Inorg. Chem.* **2016**, *55*, 488−501.

(17) Cox, N.; Retegan, M.; Neese, F.; Pantazis, D. A.; Boussac, A.; Lubitz, W. Electronic Structure of the Oxygen-Evolving Complex in Photosystem II Prior to O-O Bond Formation. *Science* **2014**, *345*, 804−808.

(18) Chu, H. A.; Hillier, W.; Law, N. A.; Sackett, H.; Haymond, S.; Babcock, G. T. Light-Induced FTIR Difference Spectroscopy of the S_2-to-S_3 State Transition of the Oxygen-Evolving Complex in Photosystem II. *Biochim. Biophys. Acta, Bioenerg.* **2000**, *1459*, 528−532.

(19) Chu, H. A.; Gardner, M. T.; O'Brie, J. P.; Babcock, G. T. Low-Frequency Fourier Transform Infrared Spectroscopy of the Oxygen-Evolving and Quinone Acceptor Complexes in Photosystem II. *Biochemistry* **1999**, *38*, 4533−4541.

(20) Noguchi, T.; Inoue, Y.; Tang, X. S. Structure of a Histidine Ligand in the Photosynthetic Oxygen-Evolving Complex as Studied by Light-Induced Fourier Transform Infrared Difference Spectroscopy. *Biochemistry* **1999**, *38*, 10187−10195.

(21) Suga, M.; Akita, F.; Hirata, K.; Ueno, G.; Murakami, H.; Nakajima, Y.; Shimizu, T.; Yamashita, K.; Yamamoto, M.; Ago, H.; Shen, J.-R. Native Structure of Photosystem II at 1.95 Resolution Viewed by Femtosecond X-ray Pulses. *Nature* **2015**, *517*, 99−103.

(22) Askerka, M.; Vinyard, D. J.; Wang, J.; Brudvig, G. W.; Batista, V. S. Analysis of the Radiation-Damage-Free X-ray Structure of Photosystem II in Light of EXAFS and QM/MM Data. *Biochemistry* **2015**, *54*, 1713−1716.

(23) Sproviero, E. M.; Gascon, J. A.; McEvoy, J. P.; Brudvig, G. W.; Batista, V. S. Quantum Mechanics/Molecular Mechanics Study of the Catalytic Cycle of Water Splitting in Photosystem II. *J. Am. Chem. Soc.* **2008**, *130*, 3428−3442.

(24) Siegbahn, P. E. M. The S_2 to S_3 Transition for Water Oxidation in PSII (Photosystem II), Revisited. *Phys. Chem. Chem. Phys.* **2018**, *20*, 22926−22931.

(25) Lohmiller, T.; Krewald, V.; Navarro, M. P.; Retegan, M.; Rapatskiy, L.; Nowaczyk, M. M.; Boussac, A.; Neese, F.; Lubitz, W.; Pantazis, D. A.; Cox, N. Structure, Ligands and Substrate Coordination of the Oxygen-Evolving Complex of Photosystem II in the S_2 State: A Combined EPR and DFT Study. *Phys. Chem. Chem. Phys.* **2014**, *16*, 11877−11892.

(26) Capone, M.; Bovi, D.; Narzi, D.; Guidoni, L. Reorganization of Substrate Waters between the Closed and Open Cubane Conformers during the S_2 to S_3 Transition in the Oxygen Evolving Complex. *Biochemistry* **2015**, *54*, 6439−6442.

(27) Tychengulova, A.; Capone, M.; Pitari, F.; Guidoni, L. Molecular Vibrations of an Oxygen-Evolving Complex and Its Synthetic Mimic. *Chem. - Eur. J.* **2019**, *25*, 13385−13395.

(28) Shen, J. R. The Structure of Photosystem II and the Mechanism of Water Oxidation in Photosynthesis. *Annu. Rev. Plant Biol.* **2015**, *66*, 23−48.

(29) Umena, Y.; Kawakami, K.; Shen, J. R.; Kamiya, N. Crystal Structure of Oxygen-Evolving Photosystem II at a Resolution of 1.9 Å. *Nature* **2011**, *473*, 55−60.

(30) Yamanaka, S.; Isobe, H.; Kanda, K.; Saito, T.; Umena, Y.; Kawakami, K.; Shen, J. R.; Kamiya, N.; Okumura, M.; Nakamura, H.; Yamaguchi, K. Possible Mechanisms for the O−O Bond Formation in Oxygen Evolution Reaction at the $CaMn_4O_5(H_2O)_4$ Cluster of PSII Refined to 1.9 Å X-ray Resolution. *Chem. Phys. Lett.* **2011**, *511*, 138−145.

(31) Siegbahn, P. E. M. Water Oxidation Mechanism in Photosystem II, Including Oxidations, Proton Release Pathways, O-O Bond Formation and O_2 Release. *Biochim. Biophys. Acta, Bioenerg.* **2013**, *1827*, 1003−1019.

(32) Zaharieva, I.; Chernev, P.; Berggren, G.; Anderlund, M.; Styring, S.; Dau, H.; Haumann, M. Room-Temperature Energy-Sampling Kβ X-ray Emission Spectroscopy of the Mn_4Ca Complex of Photosynthesis Reveals Three Manganese-Centered Oxidation Steps and Suggests a Coordination Change Prior to O_2 Formation. *Biochemistry* **2016**, *55*, 4197−4211.

(33) Suga, M.; Akita, F.; Sugahara, M.; et al. Light-Induced Structural Changes and the Site of O = O Bond Formation in PSII Caught by XFEL. *Nature* **2017**, *543*, 131−135.

(34) Suga, M.; Akita, F.; Yamashita, K.; Nakajima, Y.; Ueno, G.; Li, H.; Yamane, T.; Hirata, K.; Umena, Y.; Yonekura, S.; Yu, L.-J.; Murakami, H.; Nomura, T.; Kimura, T.; Kubo, M.; Baba, S.; Kumasaka, T.; Tono, K.; Yabashi, M.; Isobe, H.; Yamaguchi, K.; Yamamoto, M.; Ago, H.; Shen, J. R. An Oxyl/Oxo Mechanism for Oxygen-Oxygen Coupling in PSII Revealed by an X-ray Free-Electron Laser. *Science* **2019**, *366*, 334−338.

(35) Najafpour, M. M.; Zaharieva, I.; Zand, Z.; Maedeh Hosseini, S.; Kouzmanova, M.; Holynska, M.; Tranca, I.; Larkum, A. W.; Shen, J.-R.; Allakhverdiev, S. I. Water-Oxidizing Complex in Photosystem II: Its structure and Relation to Manganese-Oxide Based Catalysts. *Coord. Chem. Rev.* **2020**, *409*, 213183.

(36) Cox, N.; Pantazis, D. A.; Neese, F.; Lubitz, W. Artificial Photosynthesis: Understanding Water Splitting in Nature. *Interface Focus* **2015**, *5*, 20150009.

(37) Chu, H. A. Fourier Transform Infrared Difference Spectroscopy for Studying the Molecular Mechanism of Photosynthetic Water Oxidation. *Front. Plant Sci.* **2013**, *4*, 146.

(38) Noguchi, T.; Sugiura, M. Structure of an Active Water Molecule in the Water-Oxidizing Complex of Photosystem II As Studied by FTIR Spectroscopy. *Biochemistry* **2000**, *39*, 10943−10949.

(39) Fischer, G.; Wydrzynski, T. Isotope Effects in FTIR Difference Spectra of the Photosynthetic Oxygen-Evolving Catalytic Site Determined by ab Initio Calculations on Model Compounds. *J. Phys. Chem. B* **2001**, *105*, 12894−12901.

(40) Steenhuis, J. J.; Hutchison, R. S.; Barry, B. A. Alterations in Carboxylate Ligation at the Active Site of Photosystem II. *J. Biol. Chem.* **1999**, *274*, 14609−14616.

(41) Chu, H. A.; Gardner, M. T.; Hillier, W.; Babcock, G. T. Low-frequency Fourier Transform Infrared Spectroscopy of the Oxygen-Evolving Complex in Photosystem II. *Photosynth. Res.* **2000**, *66*, 57−63.

(42) Chu, H. A.; Hillier, W.; Law, N. A.; Babcock, G. T. Vibrational Spectroscopy of the Oxygen-Evolving Complex and of Manganese Model Compounds. *Biochim. Biophys. Acta, Bioenerg.* **2001**, *1503*, 69−82.

(43) Kanady, J. S.; Tsui, E. Y.; Day, M. W.; Agapie, T. A Synthetic Model of the Mn_3Ca Subsite of the Oxygen-Evolving Complex in Photosystem II. *Science* **2011**, *333*, 733−736.

(44) Mukherjee, S.; Stull, J. A.; Yano, J.; Stamatatos, T. C.; Pringouri, K.; Stich, T. A.; Abboud, K. A.; Britt, R. D.; Yachandra, V. K.; Christou, G. Synthetic Model of the Asymmetric $[Mn_3CaO_4]$ Cubane Core of the Oxygen-Evolving Complex of Photosystem II. *Proc. Natl. Acad. Sci. U. S. A.* **2012**, *109*, 2257−2262.

(45) Kanady, J. S.; Lin, P. H.; Carsch, K. M.; Nielsen, R. J.; Takase, M. K.; Goddard, W. A.; Agapie, T. Toward Models for the Full Oxygen-Evolving Complex of Photosystem II by Ligand Coordination To Lower the Symmetry of the Mn_3CaO_4 Cubane: Demonstration That Electronic Effects Facilitate Binding of a Fifth Metal. *J. Am. Chem. Soc.* **2014**, *136*, 14373−14376.

(46) Zhang, C.; Chen, C.; Dong, H.; Shen, J.-R.; Dau, H.; Zhao, J. A Synthetic Mn_4Ca-Cluster Mimicking the Oxygen-Evolving Center of Photosynthesis. *Science* **2015**, *348*, 690−693.

(47) Pantazis, D. A.; Ames, W.; Cox, N.; Lubitz, W.; Neese, F. Two Interconvertible Structures that Explain the Spectroscopic Properties of the Oxygen-Evolving Complex of Photosystem II in the S_2 State. *Angew. Chem., Int. Ed.* **2012**, *51*, 9935−9940.

(48) Raucci, U.; Ciofini, I.; Adamo, C.; Rega, N. Unveiling the Reactivity of a Synthetic Mimic of the Oxygen Evolving Complex. *J. Phys. Chem. Lett.* **2016**, *7*, 5015−5021.

(49) Bovi, D.; Narzi, D.; Guidoni, L. The S_2 State of the Oxygen-Evolving Complex of Photosystem II Explored by QM/MM Dynamics: Spin Surfaces and Metastable States Suggest a Reaction Path Towards the S_3 State. *Angew. Chem., Int. Ed.* **2013**, *52*, 11744−11749.

(50) Haddy, A. EPR Spectroscopy of the Manganese Cluster of Photosystem II. *Photosynth. Res.* **2007**, *92*, 357−368.

(51) Bovi, D.; Narzi, D.; Guidoni, L. Magnetic Interactions in the Catalyst Used by Nature to Split Water: a DFT + U Multiscale Study on the Mn_4CaO_5 Core in Photosystem II. *New J. Phys.* **2014**, *16*, 015020.

(52) Vass, I.; Styring, S. pH-Dependent Charge Equilibria between Tyrosine-D and the S States in Photosystem II. Estimation of Relative Midpoint Redox Potentials. *Biochemistry* **1991**, *30*, 830−839.

(53) Peloquin, J. M.; Britt, R. D. EPR/ENDOR Characterization of the Physical and Electronic Structure of the OEC Mn Cluster. *Biochim. Biophys. Acta, Bioenerg.* **2001**, *1503*, 96−111.

(54) Boussac, A.; Rutherford, A. W. Comparative Study of the g = 4.1 EPR Signals in The S_2 State of Photosystem II. *Biochim. Biophys. Acta, Bioenerg.* **2000**, *1457*, 145−156.

(55) Tsierkezos, N. G. Cyclic Voltammetric Studies of Ferrocene in Nonaqueous Solvents in the Temperature Range from 248.15 to 298.15K. *J. Solution Chem.* **2007**, *36*, 289−302.

(56) Yue, S.; Wang, Z.; Leng, X.; Zhu, R.-D.; Chen, H.-L.; Weng, Y.-X. Coupling of Multi-Vibrational Modes in Bacteriochlorophyll a in Solution Observed with 2D Electronic Spectroscopy. *Chem. Phys. Lett.* **2017**, *683*, 591−597.

(57) Longueville, W.; Fontaine, H. Diffusion Raman des Acides Pivalique Hydrogéné et Déutérie en Phase Liquide et en Solution. *J. Raman Spectrosc.* **1978**, *7*, 238−243.

(58) Maeda, A.; Ishibashi, T. A. Time-Resolved IR Observation of a Photocatalytic Reaction of Pivalic Acid on Platinized Titanium Dioxide. *Chem. Phys.* **2013**, *419*, 167−171.

(59) Bovi, D.; Capone, M.; Narzi, D.; Guidoni, L. Vibrational Fingerprints of the Mn_4CaO_5 Cluster in Photosystem II by Mixed Quantum-Classical Molecular Dynamics. *Biochim. Biophys. Acta, Bioenerg.* **2016**, *1857*, 1669−1677.

(60) Chu, H. A.; Hillier, W.; Law, N. A.; Babcock, G. T. Identification of a Possible Mn−O−Mn Cluster Vibrational Mode of the S_3 State in the Oxygen-Evolving Complex of Photosystem II by the Low-Frequency FTIR Spectroscopy. 12th International Congress on Photosynthesis, 2001; PS2001.

(61) Boussac, A.; Rutherford, A. W.; Sugiura, M. Electron Transfer Pathways from the S_2-States to the S_3-States either after a Ca^{2+}/Sr^{2+} or a Cl^-/I^- Exchange in Photosystem II from Thermosynechococcus Elongatus. *Biochim. Biophys. Acta, Bioenerg.* **2015**, *1847*, 576−586.

(62) Cox, N.; Messinger, J. Reflections on Substrate Water and Dioxygen Formation. *Biochim. Biophys. Acta, Bioenerg.* **2013**, *1827*, 1020−1030.

(63) Capone, M.; Narzi, D.; Bovi, D.; Guidoni, L. Mechanism of Water Delivery to the Active Site of Photosystem II along the S_2 to S_3 Transition. *J. Phys. Chem. Lett.* **2016**, *7*, 592−596.

(64) Kimura, Y.; Mizusawa, N.; Ishii, A.; Yamanari, T.; Ono, T. A. Changes of Low-Frequency Vibrational Modes Induced by Universal ^{15}N- and ^{13}C- Isotope Labeling in S_2/S_1 FTIR Difference Spectrum of Oxygen-Evolving Complex. *Biochemistry* **2003**, *42*, 13170−13177.

(65) Pokhrel, R.; Brudvig, G. W. Oxygen-Evolving Complex of Photosystem II: Correlating Structure with Spectroscopy. *Phys. Chem. Chem. Phys.* **2014**, *16*, 11812−11821.

https://doi.org/10.1021/acs.jpclett.1c02689
J. Phys. Chem. Lett. 2021, 12, 9830−9839

(66) Debus, R. J. FTIR Studies of Metal Ligands, Networks of Hydrogen Bonds, and Water Molecules near the Active Site Mn_4CaO_5 Cluster in Photosystem II. *Biochim. Biophys. Acta, Bioenerg.* **2015**, *1847*, 19−34.

(67) Hasegawa, K.; Ono, T.; Inoue, Y.; Kusunoki, M. How to Evaluate the Structure of a Tetranuclear Mn Cluster from Magnetic and EXAFS Data: Case of the S_2-state Mn-Cluster in Photosystem II. *Bull. Chem. Soc. Jpn.* **1999**, *72*, 1013−1023.

(68) Chu, H. A.; Sackett, H.; Babcock, G. T. Identification of a Mn-O-Mn Cluster Vibrational Mode of the Oxygen-Evolving Complex in Photosystem II by Low-Frequency FTIR Spectroscopy. *Biochemistry* **2000**, *39*, 14371−14376.

https://doi.org/10.1021/acs.jpclett.1c02689
J. Phys. Chem. Lett. 2021, 12, 9830−9839